A boundary element approach for image-guided near-infrared absorption and scatter estimation

Subhadra Srinivasan,[a] Brian W. Pogue, Colin Carpenter,
Phaneendra K. Yalavarthy, and Keith Paulsen
Thayer School of Engineering, Dartmouth College, Hanover, New Hampshire 03755

(Received 18 May 2007; revised 20 August 2007; accepted for publication 19 September 2007; published 29 October 2007)

Multimodality NIR spectroscopy systems offer the possibility of region-based vascular and molecular characterization of tissue *in vivo*. However, computationally efficient 3D image reconstruction algorithms specific to these image-guided systems currently do not exist. Image reconstruction is often based on finite-element methods (FEMs), which require volume discretization. Here, a boundary element method (BEM) is presented using only surface discretization to recover the optical properties in an image-guided setting. The reconstruction of optical properties using BEM was evaluated in a domain containing a 30 mm inclusion embedded in two layer media with different noise levels and initial estimates. For 5% noise in measurements, and background starting values for reconstruction, the optical properties were recovered to within a mean error of 6.8%. When compared with FEM for this case, BEM showed a 28% improvement in computational time. BEM was also applied to experimental data collected from a gelatin phantom with a 25 mm inclusion and could recover the true absorption to within 6% of expected values using less time for computation compared with FEM. When applied to a patient-specific breast mesh generated using MRI, with a 2 cm ductal carcinoma, BEM showed successful recovery of optical properties with less than 5% error in absorption and 1% error in scattering, using measurements with 1% noise. With simpler and faster meshing schemes required for surface grids as compared with volume grids, BEM offers a powerful and potentially more feasible alternative for high-resolution 3D image-guided NIR spectroscopy. [DOI: 10.1118/1.2795832]

Key words: near-infrared (NIR)

I. INTRODUCTION

NIR tomography is evolving as a potential complement to conventional imaging modalities such as MRI, mammography and ultrasound.[1–6] NIR imaging has the ability to provide information on the vascular and molecular architecture of tissue noninvasively which can be used for diagnosis of breast cancer.[7–9] However, the fundamental limitation of NIR imaging as a standalone modality is its poor spatial resolution arising from high scattering of light in tissues. Hence, its clinical utility may be limited without additional information from other imaging methods. There is interest in using MRI together with NIR for breast cancer diagnosis and tracking response to therapy.[1,6] An integrated system with NIR as a complement to MRI could yield additional contrast-enhancing features that may reduce false-positives and the number of follow-up invasive procedures. At the same time, high resolution MRI can guide the optical NIR image reconstruction. In this framework, NIR tomography would function as image-guided spectroscopy where suspicious regions are isolated by MR and the NIR spectroscopy is used to characterize the optical properties of these volumes of interest.

Algorithms that incorporate anatomical structure from another imaging modality such as MRI have been reported[10–15] and can be classified as those that use either soft or hard priors. Soft priors invoke a regularization term to implement MR region information and reconstruct all pixels in the mesh.[10,13,14] The approach has been considered in deterministic[10] and Bayesian[12] settings based on linear and nonlinear iterative inverse solutions. It is easily applied in two dimensions but becomes much more time consuming and severely under-determined in three dimensions due to the large number of unknowns. It is possible to improve the efficiency of the scheme through a Moore–Penrose inversion[16] but the problem is still computationally intensive. Hard priors involve the reconstruction of piecewise constant regions where the optical images are constrained to have a structure predefined by MRI.[15–17] The technique assumes the domain to consist of several homogeneous regions where the optical properties are updated uniformly such that the number of degrees of freedom in the reconstruction is dramatically reduced which stabilizes the estimation. This is especially beneficial in three dimensions because the number of unknowns can be reduced from many thousands of points (nodes) to a few piecewise constant regions (typically limited to the adipose, fibroglandular, and tumor/cyst composition of the breast). The assumption that each tissue type is homogeneous is idealized, but hard priors produce an accurate characterization of the average properties in each region even when the individual tissue constituents are complex in shape and size.[17] The approach has been implemented in 3D FEM models and shown to recover nearly 100% of the expected tumor contrast in small inclusions.[16] While hard priors provide a simple and powerful technique for incorporat-

ing MRI structure, they have typically been implemented in numerical FEM and finite difference methods (FDM) where the entire domain is discretized into volume meshes with at least 15 000 nodes (~4 mm resolution).

Here, we evaluate the potential of the boundary element method (BEM) to model light propagation in tissue and form the basis of an image reconstruction algorithm. The BEM is especially applicable when the imaging domain is homogeneous or consists of a small number of homogeneous subdomains, which is exactly the case in region-based image-guided NIR spectroscopy. An important advantage of the BEM is that it requires only surface meshes[18] as opposed to volume discretization of the entire domain as with FEM. This makes meshing a significantly simpler task because surface triangulation is much faster to generate and more reliably produced than volumetric discretization.

While optical imaging has experienced significant advances over the past two decades, the ability to perform 3D image reconstruction on a routine basis remains a formidable task. Several research groups use FEM and FDM[11,19–22] because these methods are relatively easy to deploy in two dimensions but become very time consuming in three dimensions. The BEM provides a convenient way of dealing with the meshing task by exploiting a surface discretization, which only involves triangular elements, as compared to tetrahedrons that fill the entire volume for the FEM. Adaptive meshing with spatially varying node patterns could reduce the number of nodes required to a certain extent but adds another level of complexity to the problem formulation, whereas meshing with varying resolution is substantially easier in the BEM. For example, the surface of a small tumor could be discretized independently to have higher resolution compared with the outer breast surface. Even though the BEM uses dense matrices, which are computationally intensive to solve, as compared to the sparse FEM structure, the total number of nodes in the BEM mesh is substantially smaller than its FEM counterpart.

The BEM has been applied for image reconstruction in electrical impedance tomography[23] and in impedance monitored cryosurgery.[24] This also has been studied computationally for optical tomography, to recover shape and optical coefficients in head models.[25] In this latter effort, the authors recovered the shape of a perturbation and its optical properties under the assumptions that the background values are known exactly and there was no noise in the measurements. Because the problem was geared toward reconstructing shapes of perturbations, the optical parameters were not expected to be recovered accurately. In the work presented here, the shapes of perturbations such as tumors are known *a priori* and the focus is on BEM-based reconstruction of the optical properties in different regions. This makes the problem less computationally expensive and able to handle noisy measurement data with more accurate parameter estimation. The rationale for implementing the boundary element method in this manner is for its direct applicability to 3D image recovery for MR-guided NIR systems.

This article outlines the implementation and results obtained from a BEM forward model to the diffusion equation for light propagation. It includes a comparison with existing finite element models in a multiregion imaging domain. The behavior of the BEM algorithm when subjected to various levels of measurement noise is presented along with an evaluation of its sensitivity to initial estimates of the reconstruction parameters. The reconstruction algorithm has been applied to experimental data from a phantom with an inclusion to recover the optical properties of the medium. Preliminary reconstruction results are tested on a patient-specific breast mesh generated from an MRI of a subject with a 2 m infiltrating ductal carcinoma to examine the performance with real patient data.

II. METHODS

II.A. BEM-based forward model to diffusion equation

The forward model is represented by the diffusion equation involves obtaining the light flux outgoing from different surfaces, using known optical properties for the interior of these regions. The diffusion approximation to the radiative transport equation assumes that the interior photon irradiance is highly scattered and nearly uniform in all directions, and therefore its angular distribution is effectively described by the single isotropic fluence parameter, Φ.[26] This equation is valid under the assumption that scatter dominates over absorption, which is true in the case of most tissues, including the human breast, in the wavelength region of 650–1350 nm.[27] This differential equation is written as[26,28]

$$-\nabla \cdot D(r)\,\nabla\,\Phi(r,\omega)+\left(\mu_a(r)+\frac{i\omega}{c}\right)\Phi(r,\omega)=q_0(r,\omega) \quad (1)$$

where $\Phi(r,\omega)$ is the isotropic fluence at modulation frequency ω and position r, $D(r)$ is the diffusion coefficient, $\mu_a(r)$ is the absorption coefficient, c is the speed of light in the medium, and $q_0(r,\omega)$ is an isotropic source. The diffusion coefficient can be written as

$$D(r)=\frac{1}{(3(\mu_a(r)+\mu_s'(r)))}, \quad (2)$$

where $\mu_s'(r)$ is the reduced scattering coefficient. When tissue is assumed to consist of homogeneous regions (as shown in the 2D illustration in Fig. 1), $D(r)$ is constant in each zone and for a particular frequency, ω, we can write

$$\left(\mu_a(r)+\frac{i\omega}{c}\right)=k_l^2,$$

where k_l is constant in subdomain l.[29,30] Hence, Eq. (1) can be expressed in the form of a modified Helmholtz equation

$$\nabla\,.\,D_l\,\nabla\,\Phi-k_l^2\Phi=-q_0(r,\omega), \quad (3)$$

where k_l is the wave number.

The boundary element formulation for the modified Helmholtz equation has been well detailed in literature[18] and hence the formulation for the diffusion equation under the assumption of known piecewise constant regions can be derived. The details of this derivation are presented in the Appendix, since the formulation is fairly intense mathemati-

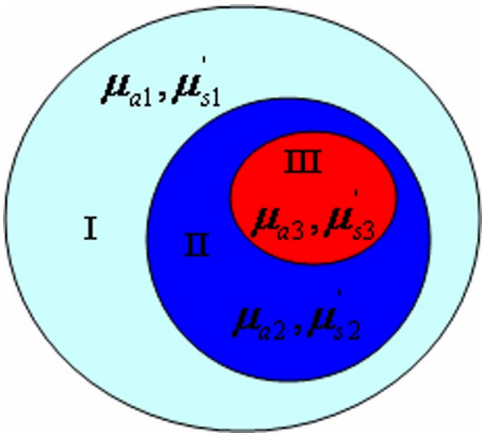

FIG. 1. (a) 2D illustration of a circular domain consisting of three homogeneous subdomains, μ_a is the absorption coefficient, and μ_s' is the reduced scattering coefficient.

cally. The breast imaging domain will typically consist of 3–4 tissue regions obtained from MRI, namely adipose and fibroglandular layers in normal tissue and additionally, malignant and benign tumor tissue in women with abnormalities. The numerical BEM framework (as detailed in the Appendix) then has to be modified to incorporate continuity conditions across these internal boundaries as shown in the Appendix.

II.B. BEM-based reconstruction of tissue optical properties

Image reconstruction is based on the BEM forward model to the diffusion equation for multiregion imaging domains as described above. The reconstruction procedure solves an inverse problem to determine the NIRS tissue vascular chromophore concentrations of oxyhemoglobin (HbO_2), deoxyhemoglobin (Hb) and water and cellular estimates of scatter amplitude and scatter power from the boundary measurements of intensity and phase after light transmittance through tissue. This also leads to derived estimates of total hemoglobin ($[Hb_T]=[HbO_2]+[Hb]$) and oxygen saturation ($S_tO_2=[HbO_2]/[Hb_T]$ in percent) as well as scatterer size and density calculated, from scatter amplitude and power using Mie theory.[31] Images of these quantities have been conventionally obtained by reconstructing optical properties at multiwavelengths initially followed by a spectral fit to estimate the chromophore concentrations and scatter parameters. Typically, image reconstruction is achieved through an iterative procedure where an objective function consisting of the difference between the measured and the modeled data is minimized. In our case, the least-squares functional to be minimized is[32]

$$\chi^2 = \sum_{j=1}^{M} (\Phi_j^{\text{meas}} - \Phi_j^{\text{cal}})^2, \tag{4}$$

where M is the total number of measurements at each wavelength, and Φ_j^{meas} and Φ_j^{cal} are the measured and calculated fluence, respectively, at the boundary for each measurement point j. The iterative procedure we used is based on Newton's method which has been applied successfully in several inverse problems.[20,33,34] Assuming that a solution for the optical properties exists, close to an initial estimate μ_0, the Gauss–Newton method generates a new search direction or update as

$$\mathfrak{J}\,\partial\mu = \partial\Phi, \tag{5}$$

where $\partial\Phi$ refers to the change in boundary data. In Eq. (5), $\mathfrak{J}$ is the Jacobian, the matrix containing the sensitivity of the boundary data to a change in optical property μ_a and diffusion coefficient D given by $\mathfrak{J}=[\mathfrak{J}_{\mu_a};\mathfrak{J}_D]$ and $\partial\mu$ is the update in the optical properties defined as $\partial\mu=[\partial\mu_a;\partial D]$. Multiplying Eq. (5) by $\mathfrak{J}^T$ and rearranging lead to

$$\partial\mu = [\mathfrak{J}^T\mathfrak{J}]^{-1}\mathfrak{J}^T\,\partial\Phi. \tag{6}$$

We solved Eq. (6) iteratively to obtain the update in optical properties, which minimizes the difference between the measured and calculated data as indicated in Eq. (4). The Jacobian was calculated using a perturbation approach to approximate the required derivatives by perturbing either μ_a or D in each region in turn and calculating the resulting change in the boundary measurements. The structure of the Jacobian has been detailed previously.[35] We implemented Eq. (6) to reconstruct iteratively for the optical properties based on a stopping criterion of a change in projection error (given by the functional in Eq. (4) of less than 2% between successive iterations. Regularization was added for data with noise due to the ill-conditioned nature of the Hessian matrix ($\mathfrak{J}^T\mathfrak{J}$) in Eq. (6). The regularization is based on a modified Levenberg–Marquardt method,[32] and the starting value for the regularization was chosen empirically based on previous experience in this area[36] and reduced successively with iterations.

II.C. Image reconstruction with FEM

The results from the BEM forward model and image reconstruction have been compared with those obtained from our FEM approach, which has been detailed and tested in multiple simulation and phantom studies.[16,20,37,38] The region-based scheme assuming piecewise constant subdomains has also been implemented using the FEM forward model where all nodes in a region have been updated simultaneously thereby substantially reducing the rank of the reconstruction basis. The FEM reconstruction uses Newton's method as described in the previous section, essentially solving the same Eq. (6). The Jacobian was also calculated using the perturbation approach for consistency in the comparison with the BEM. The stopping criterion was for change in projection error to be no less than 0.5% between successive iterations, and regularization was used to counter the ill-conditioned nature of the problem.[39] Both models use the same assumption that the imaging domain contains piecewise constant regions and use the same framework for solving the inverse problem. The differences in reconstructed results are mainly attributable to the discretization of the domain.

III. RESULTS

III.A. BEM-based forward model

Implementation of the boundary element forward model on a single homogeneous region (not shown here) produced results comparable to the finite element method, using 27% of the nodes, since only discretization of the boundary was required. The RMS difference in intensity between the two solution techniques was 0.0002 suggesting near perfect agreement between the models. Figure 2 shows results from implementation of the BEM in a two-region problem. A domain containing a single spherical inclusion of diameter 30 mm located off-center at $(0,-15,0)$ in a cylinder of diameter 86 mm and height 40 mm [shown in Fig. 2(a)] was meshed to obtain both surface and volume discretizations. Meshing was carried out using NETGEN, a freely available software package that allows surface and volumetric meshing[40,41] and automatically changes the mesh resolution near edges and curved surfaces depending on the grading desired, given the maximum mesh size. The surface grid contained triangles on the surfaces of the cylinder and the spherical anomaly [as shown in Fig. 2(b)], whereas the volume grid contained tetrahedrons throughout the volume of the cylinder such that the nodes belonging to the spherical inclusion were tagged separately to contain different optical properties. The inclusion had optical properties in 2:1 contrast with the background which had optical properties of $\mu_a=0.006\ \text{mm}^{-1}$ and $\mu_s'=1.0\ \text{mm}^{-1}$. Forward data were generated using both BEM and FEM test grids. As shown previously,[42] the FEM solution is equivalent to Monte Carlo simulation in highly scattering regime, and the model used here has been tested previously[20,35] in simulations and experiments. In order to generate accurate forward data using the FEM mesh, a high resolution test grid containing 68 360 nodes and 365 540 tetrahedrons was used. The BEM surface grid contained 3015 nodes and 6022 triangles. The imaging geometry was assumed to be a circular ring of source-detectors with 16 source-detector positions and 15 measurements collected per source location for a total of 240 measurements, as shown in Fig. 2(c).

The measurements at the detector locations for a single source are plotted in terms of log of amplitude in Fig. 2(d) and phase (in degrees) in Fig. 2(e) as a function of theta, where theta is the angle of the detector location from the source at the same plane. As expected, the intensity decreases substantially with distance away from the source. The results from the BEM forward model are comparable to the FEM generated measurements. The RMS difference in the intensity of the two solutions over all sources was found to be 4.8×10^{-5}. The difference in the two models is possibly due to differences in discretization. Phase shows a constant offset between the two models, likely due to different source implementations (Gaussian for FEM and point source for BEM). For the BEM, the source term is exactly integratable when a point description is used, as implemented here. Note that a Gaussian source integral for BEM would require volume discretization, which detracts from the most significant advantage of the BEM, namely, the need for only surface meshing.

In order to find the variation in forward data for varying resolution of meshes, the forward models for BEM and FEM were computed on three cases with varying mesh resolutions. Cases 1, 2, and 3 had resolutions of 1.5, 2, and 3 mm for FEM and 3, 4, and 5 mm for BEM meshes. All meshes were created with NETGEN as described above. The reason for the differing resolutions between BEM and FEM is that the tumor shape is significantly affected by the resolution of the volumetric mesh for FEM and hence higher resolution was required to accurately define the inclusion. This is not the case for BEM since the mesh itself describes the surface of the inclusion rather than its volume, and hence the shape is not affected to the same extent by the mesh resolution. The number of nodes for each of the test grids, along with nodes belonging to the inclusion is shown in Table I. The fraction of nodes belonging to the tumor is consistently higher in the BEM mesh. The accuracy of the forward model was quantified in terms of the RMS difference in data between the most accurate data obtained, assumed to be the forward data from the finest FEM mesh (case 1), and the current data for each of the cases from BEM and FEM. BEM was found to be more accurate at a smaller resolution compared with FEM consistently for all cases. This is in agreement with results from Fedele *et al.*[29] Figure 3 shows the overall time of computation for both models including the meshing time and the forward model computation. BEM showed a 44% to 72% improvement in computational time over FEM.

In order to characterize the computational time and memory required by the BEM as a function of mesh resolution, five different meshes were used for the same two-region domain described above [shown in Fig. 2(a)] at varying resolutions. All computations were performed on a 90 node/330 cpu Beowulf/Linux cluster with 8 GB of DDR memory per node. The memory required for the forward model was the amount (in megabytes) required to store the matrix K [given in Eq. (3)]. This is plotted on a log-log scale, as a function of the number of nodes (N) in the mesh, in Fig. 4(a). A curve-fit shows the logarithm of memory to scale linearly with logarithm of N with a slope of 1.99 such that memory scales as $\sim N^2$ as expected. The time of computation (TOC) to run the forward model is plotted as a function of the node number on a log-log scale in Fig. 4(b). A curve-fit to the data-points indicates that the time scales as $N^{2.83}$. These results agree with expectation, since the number of scalar operations in inversion should theoretically scale with the order of N^3 (or $N_2^{\log\ 7}$, to be more precise).[43]

The corresponding volumetric meshes generated for Table I were used to calculate memory and computational time for FEM forward model. A similar plot of memory required to store the stiffness matrix for FEM with respect to N, showed memory required scaling as a power function of $N^{1.02}$. This agreed with the expected theory of sparse matrix storage to scale linearly with order N .[43] Indeed BEM was found to be more memory intensive: However the ease of obtaining sur-

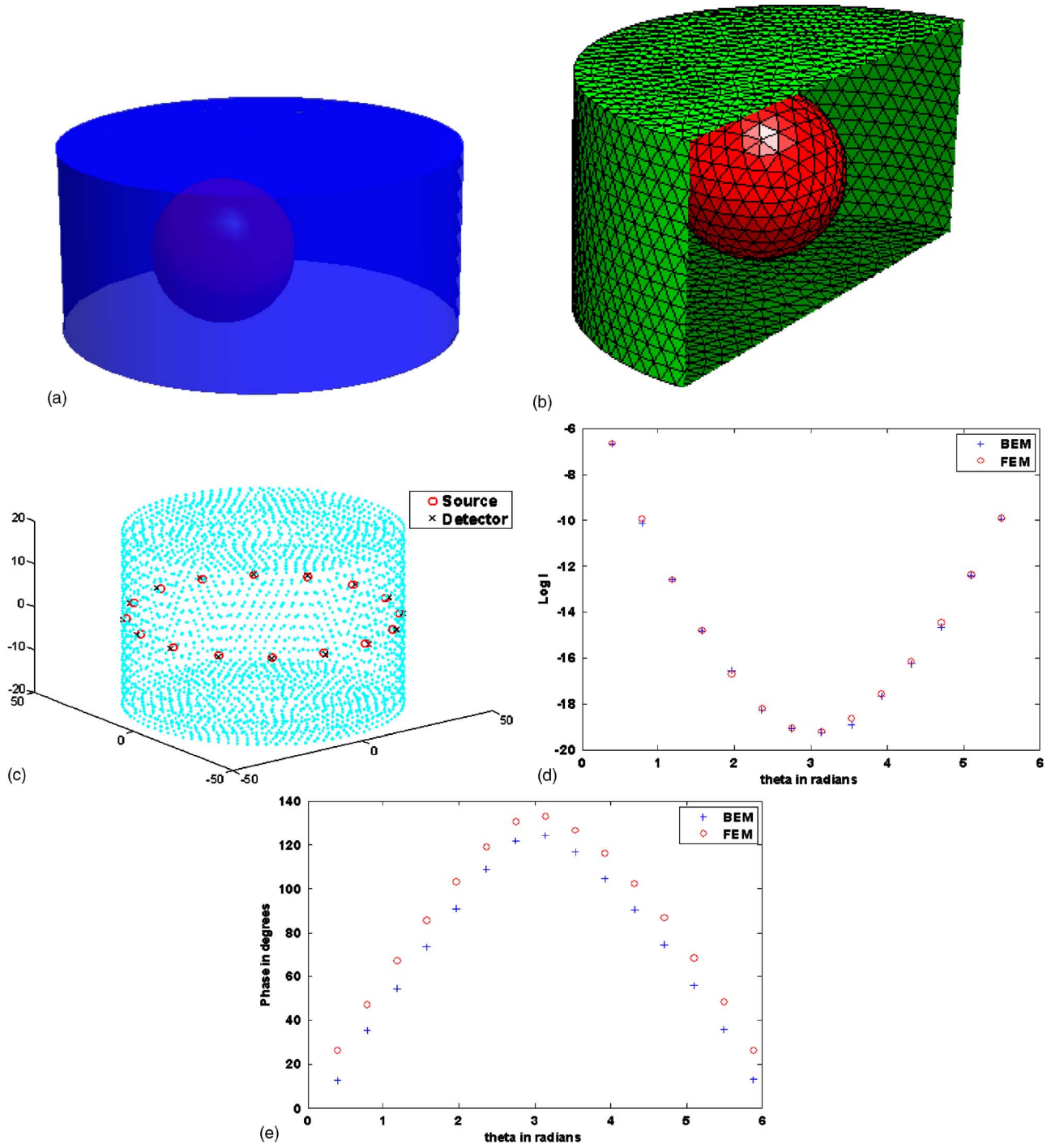

FIG. 2. (a) 3D imaging domain containing a spherical inclusion in a cylindrical domain was created for testing multiregion problem. (b) Cross section of the BEM surface mesh is shown. The size of the mesh is given in Table I (case 1). (c) Source-detector configuration for the imaging geometry is shown. (d) Comparison of the intensity at the measurement points from the FEM and BEM models on the test domain (RMS difference=0.00005) is displayed. The size of the FEM mesh is shown in Table I, case 1. (e) Comparison of phase for the two models is shown.

faces and the ability to provide accurate results with coarser representations as shown by the RMS errors compensate for this.

III.B. Reconstruction of optical properties in two-region models

The reconstruction of optical properties using the BEM forward model was implemented as described in Sec. II B. The accuracy of the reconstructions was evaluated using data generated on the imaging domain in Fig. 2(a) with 16 source-detector positions and 15 measurements collected per source location for a total of 240 measurements. This geometry is based on the NIR optical imaging system based at Dartmouth.[44] The phantom inclusion had 2:1 contrast with respect to background (background properties were $\mu_a = 0.006$ mm^{-1}, $\mu_s' = 1.0$ mm^{-1}). The forward mesh used to

TABLE I. Number of nodes in surface and volume meshes created at different resolutions for the two-region geometry shown in Fig. 2(a).

	BEM			FEM			RMS error	
Case	Node	Triangle	Node in inclusion	Node	Tetrahedron	Node in inclusion	BEM	FEM
1	3015	6022	320	68360	365540	3932	4.8×10^{-5}	-
2	1703	3398	187	32820	175002	1862	8.07×10^{-6}	3.42×10^{-5}
3	1077	2146	120	9045	44740	491	4.23×10^{-5}	9.65×10^{-4}

generate the data contained 4462 nodes and 8916 triangles and required 2.9 s for meshing. Different levels of random Gaussian distributed noise were added to the simulated data, and the optical properties were reconstructed using a different mesh containing 3015 nodes and 6033 triangles. The results are tabulated in Table II for (1) no noise in the data, (2) 1% noise in amplitude and 0.5° in phase, and (3) 5% noise in amplitude and 1° in phase. Only the recovered values in the inclusion are shown: The background value was always recovered, independent of the initial property estimates, with a mean error less than 2.5%. The starting estimate was varied from the background value to close to the true value and to an over-estimate of the true value. The error in the recovered estimates increased as the initial guess deviated from the background values. In experimental measurements, the initial estimate is obtained using a data calibration method (described in the next section), which typically yields a starting guess close to the background values. Hence starting values equal to background values (referred to as case 1, row 1 in Table II for all noise levels) along with 5% noise in measurements presents the most realistic setting for reconstruction. The average error for all noise conditions for case 1 was 1.4% in absorption and 12.2% in scattering.

To compare the performance of the BEM reconstruction with FEM-based reconstruction, a volume mesh for the domain was created using NETGEN[40,41] and contained 68 360 nodes and 365 540 tetrahedrons and required 404 s for meshing. Forward data were generated on this mesh, and 5% random Gaussian noise was added. The starting values equaled the background values, and the reconstruction for the optical properties was performed using a mesh containing 32 820 nodes and 175 002 tetrahedrons. Figure 5(a) shows the comparison of the recovered values for the absorption and scattering coefficients along with the computational time required by both FEM and BEM for processing. BEM and FEM show comparable recovery of optical properties. BEM was slightly more accurate in recovery of absorption (1.5% compared to 4% error) and less accurate in scattering (12% compared to 4%). It is expected that the use of spectral priors[45] will improve the scattering estimates. Overall, BEM took less time with an improvement of 28% in the time of

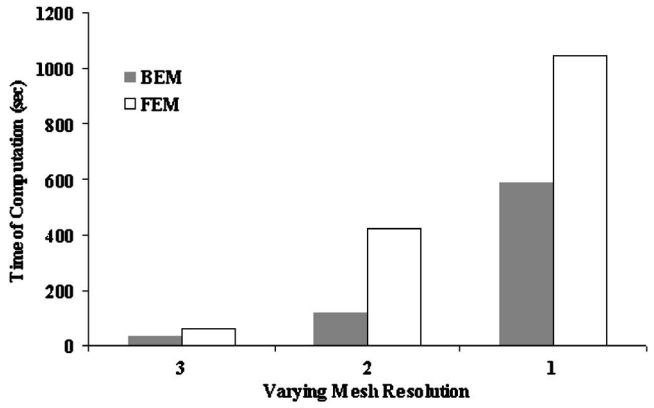

FIG. 3. Comparison of the total time of computation (meshing+forward model) required by BEM and FEM for three different cases of varying resolution of mesh is plotted. The size of the meshes for the three cases is shown in Table I.

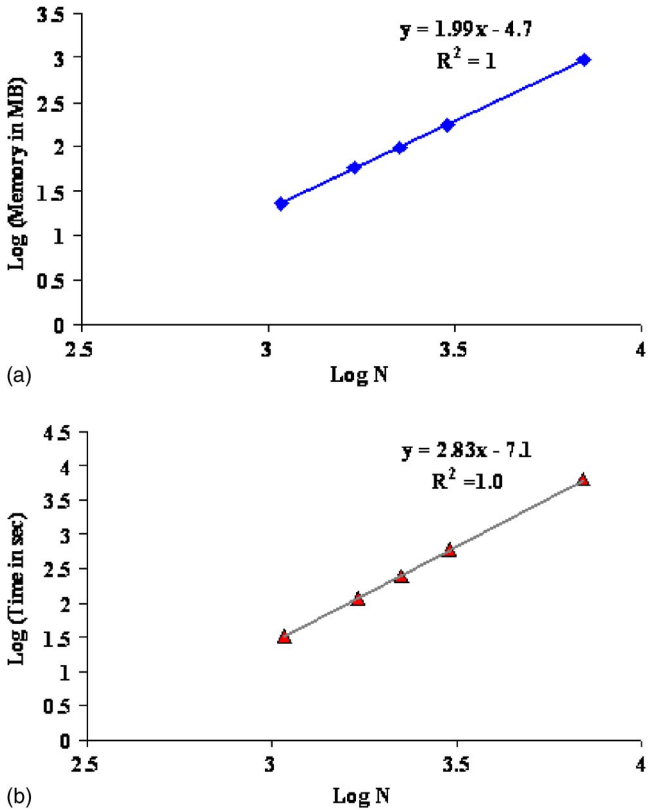

FIG. 4. (a) Logarithm of memory (in megabytes) required by the BEM forward model for the two-layer geometry as a function of the logarithm of the number of nodes (N) in the mesh. The curve fit shows that memory scales as $N^{1.99}$. (b) Logarithm of the time of computation (TOC) for the forward model as a function of the mesh size (in terms of logarithm of node number N). A fit to the data-points illustrates a linear fit with slope of 2.83 indicating that TOC scales as $N^{2.83}$. The computation time is based on a circular ring imaging geometry with 16 sources with 15 detectors per source.

TABLE II. Reconstructed values of absorption coefficient (μ_a) and reduced scattering coefficient (μ_s') in a 30mm inclusion for various levels of measurement noise in measurements starting estimates. The expected values are μ_a=0.012 mm^{-1} and μ_s'=2.0 mm^{-1}. The overall % error is the average of the errors in estimation of absorption and scattering.

Without noise				
Starting value		Reconstructed value		Overall
μ_a (mm^{-1})	μ_s' (mm^{-1})	μ_a (mm^{-1})	μ_s' (mm^{-1})	% Error
0.006	1.00	0.012	2.43	11.4
0.010	1.00	0.014	2.23	13.3
0.015	1.50	0.014	2.19	13.9
With noise: 1% noise in intensity and 0.5° in phase				
Starting value		Reconstructed value		Overall
μ_a (mm^{-1})	μ_s' (mm^{-1})	μ_a (mm^{-1})	μ_s' (mm^{-1})	% Error
0.006	1.00	0.012	2.42	11.2
0.010	1.00	0.014	2.22	13.2
0.015	1.50	0.014	2.17	13.7
With noise: 5% noise in intensity and 1° in phase				
Starting value		Reconstructed value		Overall
μ_a (mm^{-1})	μ_s' (mm^{-1})	μ_a (mm^{-1})	μ_s' (mm^{-1})	% Error
0.006	1.00	0.012	2.24	6.8
0.010	1.00	0.014	2.19	12.1
0.015	1.50	0.014	2.14	12.7

computation. The convergence with BEM was faster (four iterations) whereas FEM converged more slowly taking 20 iterations.

III.C. Experimental validation of BEM

In order to test the BEM reconstruction with experimental measurements, we used amplitude and phase data collected from a cylindrical phantom with a single inclusion. The phantom was made of gelatin with whole blood for absorption and titanium dioxide for scatter.[46] Two such gelatin phantoms with diameters of 82 mm were formed from the same mixture. One was maintained in its homogeneous state while the other had a 25 mm hole created 10 mm from the boundary. Figure 6(a) shows a photograph of the two phantoms. The hole in the second phantom was filled with a saline solution containing 3% porcine blood (the hematocrit level of the blood was measured with a clinical co-oximeter so that the absorption was known) with 0.75% Intralipid for scattering. The scattering was expected to be nearly homogeneous because 0.75% Intralipid was measured to be similar in scattering as the background gelatin. The measurement geometry is the same as described in Sec. III B and provided 240 measurements of amplitude and phase. Figure 6(b) shows the source-detector configuration. The NIR frequency domain tomography system located at Dartmouth[44] was used to collect these measurements at the periphery of the phantom in a single plane located along the center of the phantom.

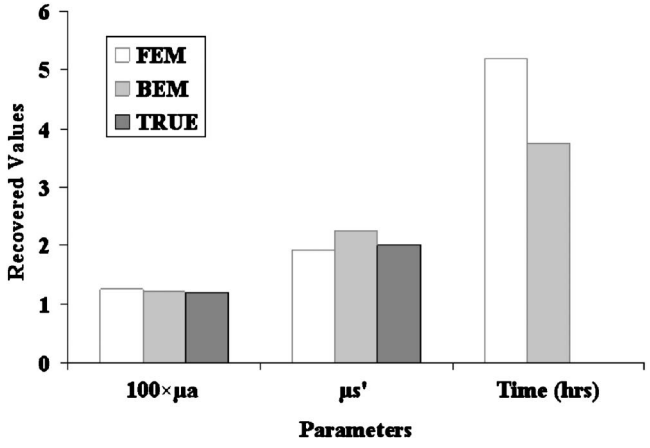

FIG. 5. (a) Comparison of the recovered absorption and scattering coefficient (in mm^{-1}) using BEM and FEM for the imaging domain shown in Fig. 2(a), as compared to the true values. The time of computation (TOC) is also shown for both methods: BEM showed an improvement in the computational time over FEM.

A cross section of the surface mesh created with NETGEN for this imaging domain is shown in Fig. 6(c). The mesh contained 2154 nodes and 4300 elements, which were deployed to produce a spatial resolution of 4 mm with moderate mesh grading. The measured data at 785 mm was calibrated using a homogeneous fitting algorithm to estimate the initial values of the absorption and scattering and scale the measurements to match the source strength in the BEM forward model. The procedure modifies raw data to account for systematic instrumentation-based offsets related to interfiber variations, source strength (i.e., multiplexing imprecision), and fiber-tissue coupling issues. A homogeneous fitting algorithm[47] is used to determine the bulk optical properties (μ_a and μ_s') for which calculated data best matches the measured data from the homogeneous calibration phantom. The details of this procedure can be found elsewhere.[47] The measured and calibrated data are plotted in Figs. 6(d) and 6(e). Using the calibrated measurements along with the surface mesh created for this geometry, the optical properties were reconstructed for the background and inclusion using the BEM. The initial estimates for the reconstruction (obtained from the fitting algorithm) as well as the reconstructed values are shown in Table III. The expected value in the inclusion was calculated from the measured hemoglobin and known extinction coefficients, to be 0.0086 mm^{-1} at 785 mm. The recovered value of absorption in the inclusion is accurate to within 6%. The expected background optical properties were estimated to be 0.0049 mm^{-1} for absorption and 0.82 mm^{-1} for scatter using measurements from the gelatin phantom maintained in the homogeneous state [shown in the top of Fig. 6(a)]. The reconstructed background in the phantom matches these results well. The reconstruction did not need regularization and converged in three iterations, requiring a total of 90 min.

For comparison, the FEM model was also used to reconstruct this data set. A volumetric mesh of the phantom containing 43 889 nodes and 237 045 tetrahedral elements was generated at 2 mm resolution with moderate mesh grading. Data calibration followed the same procedures, and back-

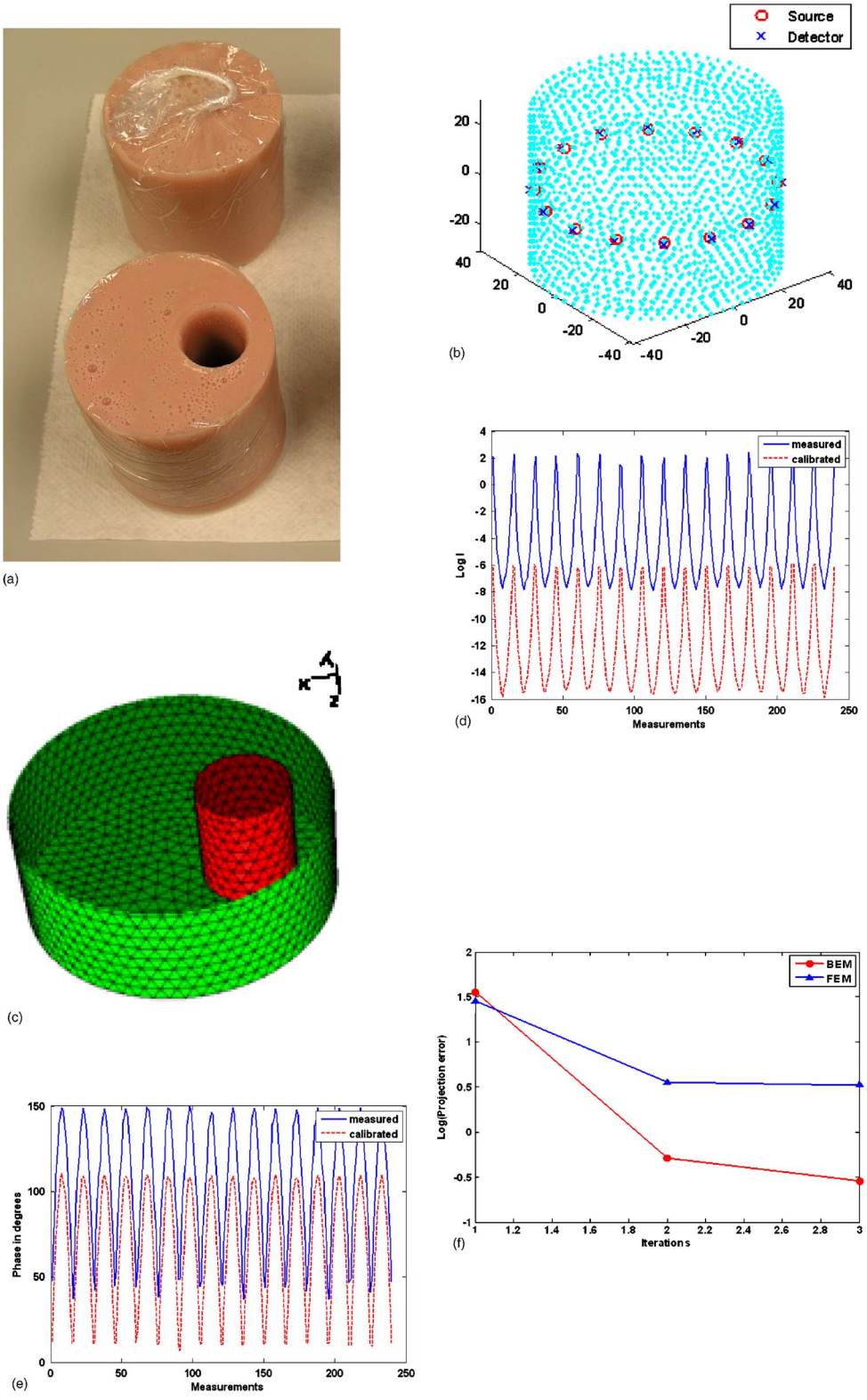

FIG. 6. (a) Photograph of two gelatin phantoms imaged with a frequency domain NIR tomography system. One was maintained in its homogeneous state while the other had an inclusion drilled and filled with a solution of Intralipid and 3% porcine blood in saline. Measurements from the latter were used to test the BEM reconstruction. (b) Surface mesh of the phantom generated with NETGEN. (c) Logarithm of the measured and calibrated intensity from the phantom. The calibration was based on an homogeneous fitting algorithm used to account for model-data mismatch. The calibrated data were used as the input to the reconstruction. (d) Phase of measured and calibrated data. (e) Logarithm of the projection error (the least-squares norm of the difference between measured and model data) as a function of iteration for the BEM and FEM reconstructions. BEM gives a lower projection error (better fit to data) compared with FEM. The reconstructed results are given in Table III.

TABLE III. Initial and reconstructed optical property values obtained from BEM and FEM inversions of experimental data collected from a gelatin phantom. Initial estimates were determined with an homogeneous fitting algorithm using the respective models. The expected value for absorption in the inclusion is 0.0086(mm^{-1}). The background values are expected to be μ_a=0.0049(mm^{-1}) and μ_s'=0.82(mm^{-1}) based on measurements in the homogeneous gelatin phantom shown in the top of Fig. 5(a).

Using BEM: BEM	μ_a (mm^{-1}) B/G	μ_a (mm^{-1}) Inclusion	μ_s' (mm^{-1}) B/G	μ_s' (mm^{-1}) Inclusion
Initial estimate	0.0050	-	0.82	-
Recovered values	0.0047	0.0091	0.81	0.71
Using FEM: FEM	μ_a (mm^{-1}) B/G	μ_a (mm^{-1}) Inclusion	μ_s' (mm^{-1}) B/G	μ_s' (mm^{-1}) Inclusion
Initial estimate	0.0055	-	0.86	-
Recovered values	0.0053	0.0081	0.88	0.81

ground values were estimated that were comparable to those obtained with the BEM (first and third rows of Table III). Using the region-based FEM reconstruction described in Sec. II C on the calibrated measurements, the optical properties of the background and inclusion were recovered. The reconstructed values are also listed in Table III. The FEM model recovered the absorption in the inclusion with a comparable error of 6%, converging in three iterations and without regularization, in 113 min. A comparison of the projection error change with iteration for the BEM and FEM reconstructions is presented in Fig. 6(f): Both methods show a decreasing trend. BEM gives a lower projection error at the last iteration when compared with FEM.

III.D. Reconstruction of optical properties on patient-specific mesh

In order to evaluate the reconstruction of optical properties in irregular imaging domains, a two-region mesh was constructed from an MR breast exam of a 29 year old subject with a 20 mm infiltrating ductal carcinoma. Specifically, 3D surfaces of the outer breast and the tumor were created from 35 MR slices of 512×512 resolution. Figure 7(a) shows a single slice of the MRI indicating the tumor location. Segmentation of the outer surface and the tumor was accomplished through the thresholding and region-growing techniques available in the Mimics™ modeling software (Materialise Inc., Leuven, Belgium[48]). Using the 3D segmented shapes, surface meshes were generated with NETGEN with a total of 2857 nodes, 318 of which were on the tumor surface. The tumor was meshed with a higher resolution than the outer breast boundary in order to preserve its shape. A contrast of 2:1 was assumed to represent the tumor relative to the background, which was assigned the optical properties μ_a=0.006 mm^{-1} and μ_a'=1.0 mm^{-1}. Simulated forward data (240 measurements from 16 source locations and 15 detectors per source) was generated on this patient-specific mesh. Figure 7(c) shows the fluence distribution for a single source on this mesh. Random Gaussian noise 1% in intensity and 0.5° in phase was added to this data set. The results from the BEM image-reconstruction for the optical properties are shown in Table IV. No regularization was required for the reconstruction and the algorithm converged in three iterations after 2.9 h of computation time.

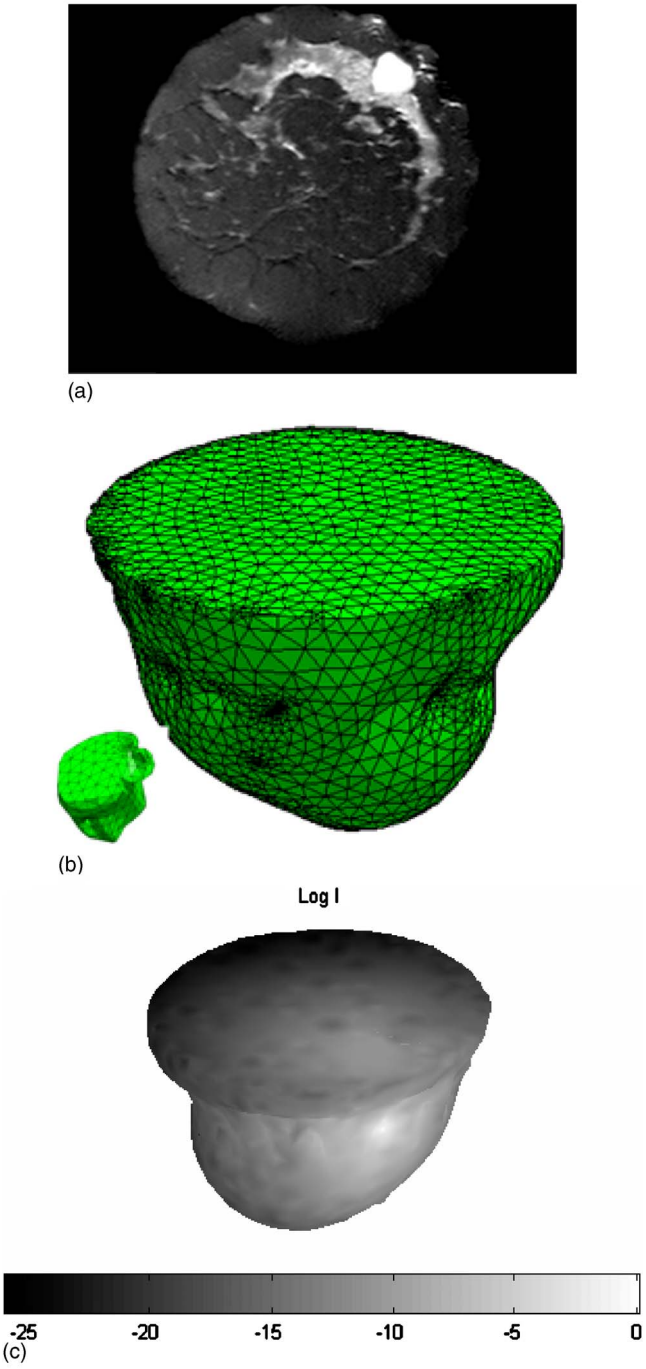

FIG. 7. (a) MR image of a patient with infilterating ductal carcinoma (indicated by the white anomaly). (b) 3D surface meshes representing the outer and tumor surfaces (not to scale) constructed from the MR image data. Measurements were simulated on this domain assuming 2:1 contrast between tumor and background. (c) Logarithm of the intensity at the boundary nodes for the BEM model. Reconstructed results for measurements generated on this domain with 1% noise are listed in Table IV.

IV. DISCUSSION

Based on the encouraging results presented here, it appears that the BEM may offer significant advantages in 3D

TABLE IV. Reconstructed values of the outer (region 1) and tumor (region 2) layers using BEM for the patient-specific domain shown in Fig. 6 with 1% noise in measurements. The values were recovered accurately with less than 5% error in absorption and 1% error in scattering.

	μ_a (mm^{-1}) B/G	μ_s' (mm^{-1}) Tumor	μ_a (mm^{-1}) B/G	μ_s' (mm^{-1}) Tumor
True values	0.006	1.0	0.012	2.0
Initial estimate	0.006	1	0.006	1.0
Recovered values	0.006	1.0	0.0126	1.98

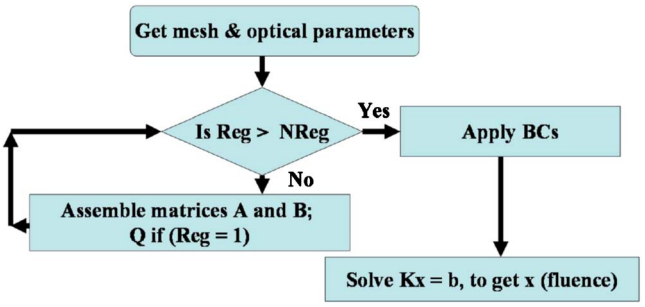

FIG. 8. Flow-chart used to solve a multiregion forward problem. Matrices A, B, Q, and K are defined in Eqs. (A5) and (A8). The outer boundary condition (BC) is type III and all internal boundaries have BCs defined by Eq. (A7).

image reconstruction. Indeed, computationally efficient tools are needed, to make well-resolved 3D NIR imaging feasible through preservation of tissue boundaries made available from high-resolution structural imaging of tissues The BEM approach to inversion provides an effective and efficient technique for solving the complex image reconstruction problem for NIR systems guided by regionized recovery of interior property parameters. The computational resources required by BEM compare favorably with FEM (Fig. 3) in a two-region imaging domain. This is particularly important because of the considerable added complexity associated with volume (required by FEM) relative to surface (required by BEM) mesh generation from medical images. Currently, the difficulty in obtaining volumetric meshes from MR images of clinical patients, tagging these meshes with material properties to allow region-based recovery of optical properties, and processing them at high resolution presents challenges to 3D FEM image reconstruction from a clinical workflow perspective. Even if a volume mesh could be successfully obtained, preserving the boundary information in the interior of the breast is difficult and will depend on the meshing technique used. If a volumetric mesh is created before assigning material properties to interior tissue layers, as is commonly the case, the shape of the interior structures will be significantly affected by the resolution of the mesh. This results in incorrect segmentation, leading to errors in reconstruction[11] for meshes without sufficient resolution, and suffers from high computational burden for high-resolution meshes. Adaptive meshing offers a potential alternative. However, while many commercial software packages offer the capability of adaptively meshing simple domains, many of these fail in complex domains containing the fingerlike fibroglandular structures observed in the breast tissue (Fig. 7(a)). The shape of the boundaries can be preserved much more easily when using surfaces allowing more accurate representation of the imaging domain. Volume meshing is a complicated problem and by moving to surface-based discretization for the parameter-reduction problem using the BEM approach, as in the case of image-guided spectroscopy, it is possible to gain significantly in computational efficiency, accuracy, and feasibility.

The main disadvantage associated with BEM is that it uses full matrices compared with FEM, which uses sparse matrices. The size of the mesh for BEM is smaller than for FEM, so this compensates for the matrix computational burden; however this advantage reduces as the surface to volume ratio increases. The complexity of the BEM problem also increases with the number of subregions, and this method is ideally suited when the domain is limited in the number of homogeneous zones to reconstruct for. In the setting of breast imaging, this can be approximated to 2–4 layers when including adipose, fibroglandular, malignant, and/or benign lesions providing a realistic scenario to apply BEM.

Field solutions generated using BEM were nearly identical to those obtained with FEM. Specifically, an RMS difference of 0.00005 was found in the two solutions for a two-region imaging domain, and this difference is likely due to differences in the mesh creation and the source implementation, rather than fundamental accuracy differences between the two methods. The BEM forward model was also used along with an iterative Newton's method to reconstruct the optical properties in a two-region domain. For a 30 mm inclusion, the properties could be recovered accurately with less than 14% error overall for different initial estimates, from measurements with up to 5% noise. In comparison to FEM results for the 5% noise case, BEM showed improvement in absorption recovery (mean error of 1.4% when compared with 4% from FEM) while taking lesser time for computation (=0.72 × time for FEM computation) .

BEM reconstruction was applied to experimental data collected from a gelatin phantom with a single inclusion. The recovered absorption was accurate to within 94% of the expected value of the inclusion, and demonstrated similar contrast recovery as FEM, with a 25% improvement in the time of computation. Scattering should have been homogeneous: BEM reconstructed a contrast of 10% similar to the trend observed with FEM. The use of spectral priors is expected to improve the accuracy of scatter recovery[9] and will be examined in future studies. Both methods used identical imaging domains and Newton's method without regularization; hence the differences in the reconstructed values are probably due to differences in mesh resolution.

The potential of BEM to recover properties within irregular geometries was examined through a patient-specific mesh generated from breast MR images. The mesh contained a 20 mm tumor segmented from the MRI. Using simulated measurements with 1% noise, we successfully reconstructed the optical properties with less than 5% error in absorption and

1% error in scattering. The FEM reconstruction on this patient-specific mesh was not evaluated due to the practical difficulties associated with the mesh generation and processing at high resolution. This is an example of a case where the geometric complexity of the breast would limit the use of FEM to accurately recover the optical properties because of the very high resolution required to represent the geometry whereas the need of only a surface mesh makes the problem much more tractable by using BEM.

BEM provides a feasible and efficient method for region-based 3D reconstruction of optical properties for image-guided-NIRS. While the complexity of the BEM problem will increase with the number of subregions defined within the imaging domain, it provides a valuable approach to imaging at millimeter resolution. In future investigations, we will extend the image reconstruction to more regions and apply it to clinical data. It may be possible to speed up the reconstruction procedure using an analytical formulation for the Jacobian matrix[49] and this will be attempted in the future. We will also explore the direct reconstruction of functional parameters through the use of spectral constraints along with data from multiwavelengths.

ACKNOWLEDGMENTS

This work was funded by the National Cancer Institute through Grants PO1CA80139 and 1U54CA105480 (Subcontract No. 2003-1344) and from ART Inc., Montreal, Quebec, Canada.

APPENDIX: DETAILS OF BEM FORMULATION

The Green's function for the modified Helmholtz equation satisfies

$$D_l\nabla^2 G(r,r_i) - k_l^2 G(r,r_i) = -\delta(r-r_i), \tag{A1}$$

and has the general solution[50]

$$G_i(r,r_i) = \frac{\exp\left(\frac{-k_l|r-r_i|}{\sqrt{D_l}}\right)}{4\pi D_l|r-r_i|}, \quad \text{in three dimensions..} \tag{A2}$$

The boundary element formulation for Eq. (3) can be shown to be

$$c_i\Phi_i + \oint D_l\frac{\partial G_i}{\partial n}\Phi - \oint D_l\frac{\partial \Phi}{\partial n}G_i = \langle q_0, G_i\rangle, \tag{A3}$$

where $c_i=\{\frac{\Omega}{4\pi}$, three dimensions , Ω is the solid angle enclosed by the boundary at node i,[50] and $\oint$ is the integral over the boundary. Discretizing Eq.(A3) through the linear basis function ψ such that

$$\Phi = \sum_{i=1}^{N}\Phi_i\psi_i \quad \text{and} \quad D_l\frac{\partial\Phi}{\partial n} = \sum_{i=1}^{N} D_l\frac{\partial\Phi_i}{\partial n}\psi_i,$$

where N is the number of nodes, produces

$$c_i\Phi_i + \sum_{i=1}^{N}\Phi_i\oint D_l\frac{\partial G_i}{\partial n}\psi_j ds - \sum_{i=1}^{N} D_l\frac{\partial\Phi_i}{\partial n}\oint G_i\psi_j ds = \langle q_0, G_i\rangle. \tag{A4}$$

In matrix form, Eq. (A4) becomes

$$[A]\{\Phi_i\} - [B]\left\{D_l\frac{\partial\Phi_i}{\partial n}\right\} = \{Q_i\}, \tag{A5}$$

where

$$A_{i,j} = c_i\delta_{ij} + \oint D_l\frac{\partial G_i}{\partial n}\psi_j ds,$$

$$B_{ij} = \oint G_i\psi_j ds,$$

$$Q_i = \langle q_0, G_i\rangle.$$

We have used a point source representation of q_0 placed one scattering distance inside the outer boundary. This simplifies the source term integral, which becomes analytic.[29] Equation (A5) is the discretized forward model, which is implemented with a type III boundary condition on the outer boundary a given by

$$\Phi_{aI} + \frac{D_I}{\alpha}\left.\frac{\partial\Phi}{\partial n}\right|_{aI} = 0, \tag{A6}$$

where α is the term incorporating the refractive index mismatch at the boundary.

Multiregion problems

For a three-region problem, as depicted in Fig. 1, the continuity conditions for boundary m (any internal interface) separating regions l and $l-1$ are written as

$$\Phi_{m(l-1)} = \Phi_{ml},$$
$$D_{(l-1)}\left.\frac{\partial\Phi}{\partial n}\right|_{m(l-1)} = -D_l\left.\frac{\partial\Phi}{\partial n}\right|_{ml}. \tag{A7}$$

Figure 8 shows a flow-chart for solving the multiregion forward problem where matrices A and B are defined in Eq. (A5) and matrix K for a three-region problem, written as $Kx=b$, has the form

$$\begin{bmatrix} (A_{11I}+\alpha B_{11I}) & A_{12I} & -B_{12I} & 0 & 0 \\ (A_{21I}+\alpha B_{21I}) & A_{22I} & -B_{22I} & 0 & 0 \\ 0 & A_{22II} & B_{22II} & A_{23II} & -B_{23II} \\ 0 & A_{32II} & B_{32II} & A_{33II} & -B_{33II} \\ 0 & 0 & 0 & A_{33III} & B_{33III} \end{bmatrix} \times \begin{Bmatrix} \Phi_{1I} \\ \Phi_{2I} \\ D_I \left.\frac{\partial \Phi}{\partial n}\right|_{2I} \\ \Phi_{3II} \\ D_{II} \left.\frac{\partial \Phi}{\partial n}\right|_{3II} \end{Bmatrix} = \begin{Bmatrix} Q_{1I} \\ Q_{2I} \\ 0 \\ 0 \\ 0 \end{Bmatrix}. \quad \text{(A8)}$$

The subscripts 1, 2, and 3 denote the outer and inner nested boundaries of the regions shown in Fig. 1(a). This relationship reveals that K is a banded matrix, which can easily be extended to any number of regions. The matrix relationship can be suitably derived for non-nested regions as well. The source contribution was assumed to exist only in the outermost region.

[a]Author to whom correspondence should be addressed. Electronic mail: subha@dartmouth.edu Telephone: 603-646-2119; Fax: 603-646-3699.

[1]B. Brooksby *et al.*, "Imaging breast adipose and fibroglandular tissue molecular signatures using hybrid MRI-guided near-infrared spectral tomography," Proc. Natl. Acad. Sci. U.S.A. **103**, 8828–33 (2006).
[2]V. Ntziachristos *et al.*, "MRI-guided diffuse optical spectroscopy of malignant and benign breast lesions," Neoplasia **4**, 347–354 (2002).
[3]Q. Zhang *et al.*, "Coregistered tomographic x-ray and optical breast imaging: initial results," J. Biomed. Opt. **10**, 024033-1–9 (2005).
[4]Q. Zhu, E. Conant, and B. Chance, "Optical imaging as an adjunct to sonograph in differentiating benign from malignant breast lesions," J. Biomed. Opt. **5**, 229–236 (2000).
[5]G. Gulsen *et al.*, "Congruent MRI and near-infrared spectroscopy for functional and structural imaging of tumors," Technol. Cancer Res. Treat. **1**, 1–9 (2002).
[6]C. Carpenter *et al.*, "Image-guided optical spectroscopy provides molecular-specific information in vivo: MRI-guided spectroscopy of breast cancer hemoglobin, water, and scatterer size," Opt. Lett. **32**, 933–935 (2007).
[7]B. Chance *et al.*, "Breast cancer detection based on incremental biochemical and physiological properties of breast cancers: a six-year, two-site study," Acad. Radiol. **12**, 925–933 (2005).
[8]B. J. Tromberg *et al.*, "Imaging in breast cancer: diffuse optics in breast cancer: detecting tumors in pre-menopausal women and monitoring neoadjuvant chemotherapy," Breast Cancer Res. **7**, 279–285 (2005).
[9]S. Srinivasan *et al.*, "Near-infrared characterization of breast tumors in-vivo using spectrally-constrained reconstruction," Technol. Cancer Res. Treat. **4**, 513–526 (2005).
[10]B. Brooksby *et al.*, "Combining near infrared tomography and magnetic resonance imaging to study *in vivo* breast tissue: implementation of a Laplacian-type regularization to incorporate MR structure," J. Biomed. Opt. **10**, 051504–1:10 (2005).
[11]G. Boverman *et al.*, "Quantitative spectroscopic diffuse optical tomography of the breast guided by imperfect a priori structural information," Phys. Med. Biol. **50**, 3941–3956 (2005).
[12]M. Guven *et al.*, "Diffuse optical tomography with apriori anatomical information," Phys. Med. Biol. **50**, 2837–2858 (2005).
[13]X. Intes *et al.*, "Diffuse optical tomography with physiological and spatial a priori constraints," Phys. Med. Biol. **49**, N155–N162 (2004).
[14]A. Li *et al.*, "Optimal linear inverse solution with multiple priors in diffuse optical tomography," Appl. Opt. **44**, 1948–1956 (2005).
[15]M. Schweiger and S. R. Arridge, "Optical tomographic reconstruction in a complex head model using apriori region boundary information," Phys. Med. Biol. **44**, 2703–2721 (1999).
[16]H. Dehghani *et al.*, "Three-dimensional optical-tomography: resolution in small-object imaging," Appl. Opt. **42**, 3117–3128 (2003).
[17]B. Brooksby, H. Dehghani, B. W. Pogue, and K. D. Paulsen, "Near infrared (NIR) tomography breast image reconstruction with *a priori* structural information from MRI: algorithm development for reconstructing heterogeneities," IEEE J. Sel. Top. Quantum Electron. **9**, 199–209 (2003).
[18]C. A. Brebbia and J. Dominguez, *Boundary Elements: An Introductory Course* (Computational Mechanics Publications, Southampton, Boston, 1992).
[19]S. R. Arridge and M. Schweiger, "Image reconstruction in optical tomography," Philos. Trans. R. Soc. London, Ser. B **352**, 717–726 (1997).
[20]K. D. Paulsen and H. Jiang, "Spatially varying optical property reconstruction using a finite element diffusion equation approximation," Med. Phys. **22**, 691–701 (1995).
[21]A. H. Hielscher, A. D. Klose, and K. M. Hanson, "Gradient-based iterative image reconstruction scheme for time-resolved optical tomography," IEEE Trans. Med. Imaging **18**, 262–271 (1999).
[22]M. Schweiger, S. R. Arridge, and I. Nissila, "Gauss-Newton method for image reconstruction in diffuse optical tomography," Phys. Med. Biol. **50**, 2365–2386 (2005).
[23]S. Babaeizadeh *et al.*, "Electrode boundary conditions and experimental validation for BEM-based EIT forward and inverse solutions," IEEE Trans. Med. Imaging **25**, 1180–1188 (2006).
[24]D. M. Otten and B. Rubinsky, "Front-tracking image reconstruction algorithm for EIT-monitored cryosurgery using the boundary element method," Physiol. Meas. **26**, 503–516 (2005).
[25]A. D. Zacharopoulos *et al.*, "Three-dimensional reconstruction of shape and piecewise constant region values for optical tomography using spherical harmonic parametrization and a boundary element method," Inverse Probl. **22**, 1509–1532 (2006).
[26]A. Ishimaru, *Wave propagation and scattering in random media* (Academic Press, Inc., New York, 1978), Vol. 1.
[27]M. S. Patterson, B. C. Wilson, and D. R. Wyman, "The propagation of optical radiation in tissue II. Optical properties of tissues and resulting fluence distributions," Lasers Med. Sci. **6**, 379–390 (1991).
[28]T. J. Farrell, M. S. Patterson, and B. C. Wilson, "A diffusion theory model of spatially resolved, steady-state diffuse reflectance for the noninvasive determination of tissue optical properties," Med. Phys. **19**, 879–888 (1992).
[29]F. Fedele *et al.*, "Fluorescence photon migration by the boundary element method," J. Comput. Phys. **210**, 109–132 (2005).
[30]J. Sikora *et al.*, "Diffuse photon propagation in multilayered geometries," Phys. Med. Biol. **51**. 497–516 (2006).
[31]X. Wang *et al.*, "Image reconstruction of effective Mie scattering parameters of breast tissue *in vivo* with near-infrared tomography," J. Biomed. Opt. **11**, 041106-1–041106-13 (2006).
[32]D. W. Marquardt, "An algorithm for least squares estimation of nonlinear parameters," J. Soc. Ind. Appl. Math. **11**, 431–441 (1963).
[33]B. Kaltenbacher, "Some Newton-type methods for the regularization of nonlinear ill-posed problems," Inverse Probl. **13**, 729–753 (1997).
[34]M. Hanke, "A regularizing Levenberg-Marquardt scheme, with applications to inverse groundwater filteration problems," Inverse Probl. **13**, 79–95 (1997).
[35]H. Dehghani, B. W. Pogue, S. P. Poplack, and K. D. Paulsen, "Multiwavelength three-dimensional near-infrared tomography of the breast: initial simulation, phantom, and clinical results," Appl. Opt. **42**, 135–145 (2003).
[36]S. Srinivasan, B. W. Pogue, H. Dehghani, S. Jiang, X. Song, and K. D. Paulsen, "Improved quantification of small objects in near-infrared diffuse optical tomography," J. Biomed. Opt. **9**, 1161–1171 (2004).
[37]T. O. McBride *et al.*, "Initial studies of *in vivo* absorbing and scattering heterogeneity in near-infrared tomographic breast imaging," Opt. Lett. **26**, 822–824 (2001).
[38]P. K. Yalavarthy *et al.*, "Weight-matrix structured regularization provides optimal generalized least-squares estimate in diffuse optical tomography," Med. Phys. **34**, 2085–2098 (2007).
[39]S. R. Arridge, "Optical tomography in medical imaging," Inverse Probl. **15**, R41–R93 (1999).
[40]J. Schöberl, http://www.hpfem.jku.at/netgen/
[41]J. Schöberl, "NETGEN–An advancing front 2D/3D-mesh generator based on abstract rules," Comput. Visualization Sci. **1**, 41–52 (1997).

[42]S. R. Arridge, M. Schweiger, M. Hiraoka, and D. T. Delpy, "A finite element approach for modeling photon transport in tissue," Med. Phys. **20**, 299–309 (1993).
[43]W. H. Press *et al.*, *Numerical Recipes in Fortran*, 2nd ed. (Cambridge University Press, New York, 1992).
[44]T. O. McBride *et al.*, "A parallel-detection frequency-domain near-infrared tomography system for hemoglobin imaging of the breast *in vivo*," Rev. Sci. Instrum. **72**, 1817–1824 (2001).
[45]S. Srinivasan, B. W. Pogue, S. Jiang, H. Dehghani, and K. D. Paulsen, "Spectrally constrained chromophore and scattering NIR tomography provides quantitative and robust reconstruction," Appl. Opt. **44**, 1858–1869 (2005).
[46]B. W. Pogue and M. S. Patterson, "Review of tissue simulating phantoms for optical spectroscopy, imaging and dosimetry," J. Biomed. Opt. **11**, 041102-1–041102-16 (2006).
[47]T. O. McBride *et al.*, "Strategies for absolute calibration of near infrared tomographic tissue imaging," Adv. Exp. Med. Biol. **531**, 85–99 (2003).
[48]Materialise, http://materialise.com/materialise/view/en/92458-Mimics.html
[49]S. Babaeizadeh, D. H. Brooks, and D. Isaacson, "3-D electrical impedance tomography for piecewise constant domains with known internal boundaries," IEEE Trans. Biomed. Eng. **54**, 2–10 (2007).
[50]C. A. Brebbia and S. Walker, *Boundary Element Techniques in Engineering* (Newnes-Butterworths, London, 1980).